

New bounds on Axion-Like Particles in the Ultraviolet from Legacy Data

Elisa Todarello

School of Physics and Astronomy, University of Nottingham, University Park, NG7 2RD, Nottingham, United Kingdom

E-mail: elisa.todarello@nottingham.ac.uk

Abstract. We use legacy data from the Hubble Space Telescope (HST) and the International Ultraviolet Explorer (IUE) to search for a spectral line from the spontaneous decay of axion-like particle (ALP) dark matter. The HST data consists of blank sky observations taken with the Faint Object Spectrograph in the 165–240 nm wavelength range, while the IUE data consists of observations of the Virgo Cluster obtained with the long- and short-wavelength spectrographs, covering 195–325 nm and 123–200 nm, respectively. We set a 95% C.L. upper limit on the ALP–photon coupling $g_{a\gamma} < 10^{-11} \text{ GeV}^{-1}$ across the full ALP mass range. Notably, we rule out values of $g_{a\gamma}$ above $1.6 \times 10^{-12} \text{ GeV}^{-1}$ for ALP masses between 12.4 and 14.5 eV, improving upon previous limits by an order of magnitude.

Contents

1	Introduction	1
2	ALP signal	2
3	Data and Methods	3
3.1	Hubble Space Telescope (HST) Faint Object Spectrograph (FOS)	3
3.1.1	Data	3
3.1.2	Modeling of the signal	6
3.2	International Ultraviolet Explorer (IUE)	7
3.2.1	Data	7
3.2.2	Modeling of the signal	9
4	Results	11
4.1	HST FOS	12
4.2	IUE	13
5	Comparison with other work	13
6	Conclusions	15

1 Introduction

Axion-like particles (ALPs) are a compelling candidate for dark matter (DM). They are light pseudo-scalars that can be produced non-thermally in the early Universe [1], similar QCD axions [2–8]. Both QCD axions and ALPs couple to the electromagnetic field through the interaction term

$$\mathcal{L} = -\frac{1}{4}g_{a\gamma} a F_{\mu\nu}\tilde{F}_{\mu\nu} \ ,$$

where a is the ALP field, $F_{\mu\nu}$ is the electromagnetic field strength tensor, $\tilde{F}_{\mu\nu} = \epsilon^{\mu\nu\rho\sigma}F_{\rho\sigma}/2$ is its dual, and $g_{a\gamma}$ is the ALP–photon coupling constant. Through this interaction, an ALP can decay into two photons. If ALPs constitute the dark matter, their decay would produce a spectral line with a frequency equal to half the ALP mass, and a width determined by the DM momentum dispersion. The relative width of this line is of order 10^{-3} for dark matter in the Milky Way (MW) and can be broader in galaxy clusters or narrower in dwarf galaxies.

In this work, we use legacy data from the Hubble Space Telescope (HST) Faint Object Spectrograph (FOS) [9] and from the International Ultraviolet Explorer (IUE) [10] to search for such a spectral line arising from the MW and Virgo cluster halos, respectively. The HST FOS was operational from 1990 to 1997 and provided ultraviolet and optical spectra with high spatial and spectral resolution. We use data collected

in 1991–1992 from blank sky regions, acquired during the science verification phase with the goal of studying the diffuse sky background [11]. The IUE, which operated from 1978 to 1996, was one of the earliest space telescopes dedicated to ultraviolet astronomy. We use Virgo cluster observations taken with its short- and long-wavelength spectrographs in 1978, 1981, and 1988. Despite the age of these instruments, their legacy data continue to be valuable for searching for weak spectral lines from processes such as ALP decay.

The spectral line search technique employed here has been used in other works to set bounds on $g_{a\gamma}$ using spectroscopic data in the infrared [12–15], optical [16–18], and ultraviolet [19] bands. The ALP mass range between 12.4 and 14.5 eV has remained relatively unexplored, with the strongest existing bound being $1.6 \times 10^{-11} \text{ GeV}^{-1}$, derived from HST measurements of anisotropies in the cosmic optical background [20, 21]. In this work, we improve upon that limit by one order of magnitude, obtaining a bound $g_{a\gamma} < 1.6 \times 10^{-12} \text{ GeV}^{-1}$ using the HST FOS, and $g_{a\gamma} < 2.1 \times 10^{-11} \text{ GeV}^{-1}$ using the IUE short-wavelength spectrograph.

This paper is structured as follows. In Section 2, we derive expressions for the ALP decay signal, explicitly accounting for the ALP momentum distribution. In Section 3, we describe the data and the modeling of the expected signal for HST and IUE. Section 4 presents our results. In Section 5, we compare our findings to those from Ref. [22]. Finally, we conclude in Section 6.

2 ALP signal

We start by deriving an expression for ALP spontaneous decay signal starting from the Boltzmann equation. We take explicitly into account the ALP momentum distribution. A more complex version of this calculation is presented in Refs [23, 24] for the case of stimulated decay of ALPs into radio-photons. The Boltzmann equation for the ALP number density is

$$\frac{d^3 \dot{n}_a}{dk^3} = -\frac{1}{(2\pi)^3} \frac{1}{2\omega_k} \int \frac{d^3 p}{(2\pi)^3} \frac{f_a(\vec{p})}{2\omega_p} \frac{d^3 q}{(2\pi)^3} \frac{1}{2\omega_q} (2\pi)^4 \delta^{(4)}(q+k-p) |\mathcal{M}_0|^2 . \quad (2.1)$$

Here p is the ALP 4-momentum, with $p^0 = \omega_p = \sqrt{m_a^2 + \vec{p}^2}$, where m_a is the ALP mass. The 4-momenta of the two photons produced in the decay are k and q , with $k^0 = \omega_k = |\vec{k}|$. The matrix element squared $|\mathcal{M}_0|^2$ is summed over the polarizations of the two photons and including a factor of 1/2 for identical particles in the final state. We assume that the ALP phase-space distribution is locally a Maxwell-Boltzmann, with an isotropic location-dependent width $\delta p(\vec{x})$ and no net DM average momentum. The ALP DM phase space density is then

$$f_a(\vec{p}, \vec{x}) = n_a(\vec{x}) \frac{(2\pi)^3}{(2\pi)^{3/2} \delta p(\vec{x})^3} e^{-\frac{\vec{p}^2}{2\delta p(\vec{x})^2}} . \quad (2.2)$$

The axion number density is given by

$$n_a(\vec{x}) = \int \frac{d^3 p}{(2\pi)^3} f_a(\vec{p}, \vec{x}) . \quad (2.3)$$

Assuming ALPs are non-relativistic, we can neglect the ALP momentum everywhere in Eq. (2.1), except within the Dirac delta function and $f_a(\vec{p})$. After simple manipulations, we obtain the rate of change of the ALP number density per unit frequency and unit solid angle

$$\frac{d\dot{n}_a}{d\nu d\Omega_k} = -\Gamma_a n_a h_\nu(\delta p) \quad h_\nu(\delta p) = \frac{1}{\sqrt{2\pi}\delta p} e^{-\frac{\epsilon^2}{2\delta p^2}} , \quad (2.4)$$

where $\nu = \omega_k/(2\pi)$, $\epsilon = 4\pi\nu - m_a$, and $\Gamma_a = g_{a\gamma}^2 m_a^3/(64\pi)$ is the ALP decay rate. Notice that $h_\nu(\delta p)$ reduces to a Dirac-delta $\delta(\epsilon)$ for $\delta p \rightarrow 0$.

Each of the two decay photons carries an energy approximately equal to $m_a/2$. Then, integrating along the line of sight ℓ , we obtain the spectral intensity as

$$I_\nu = \int d\ell 2 \frac{m_a}{2} \left| \frac{d\dot{n}_a}{d\nu d\Omega_k} \right| e^{-\tau_\nu} , \quad (2.5)$$

where τ_ν is the optical depth at frequency ν . Integrating I_ν over the observing beam solid angle $B_\nu(\Omega)$, we obtain the flux density

$$S_\nu = \Gamma_a \int d\ell \int d\Omega B_\nu(\Omega) \rho_a(\vec{x}(\ell, \Omega)) h_\nu(\delta p(\vec{x}(\ell, \Omega))) e^{-\tau_\nu(\vec{x}(\ell, \Omega))} , \quad (2.6)$$

where ρ_a is the dark matter energy density.

We can now calculate the average flux density in a frequency bin of width $\Delta\nu$ centered at ν_0 . Defining $\epsilon_0 = 4\pi\nu_0 - m_a$, and assuming the beam and the optical depth don't vary appreciably over the bin width. We obtain

$$\begin{aligned} \langle S_\nu \rangle &= \frac{1}{\Delta\nu} \int_{\nu_0 - \frac{\Delta\nu}{2}}^{\nu_0 + \frac{\Delta\nu}{2}} d\nu S_\nu = \Gamma_a \int d\ell d\Omega B_{\nu_0} \rho_a e^{-\tau_{\nu_0}} \\ &\quad \times \frac{1}{8\pi\Delta\nu} \left[\operatorname{erf} \left(\frac{\epsilon_0 + 2\pi\Delta\nu}{\sqrt{2}\delta p} \right) - \operatorname{erf} \left(\frac{\epsilon_0 - 2\pi\Delta\nu}{\sqrt{2}\delta p} \right) \right] \end{aligned} \quad (2.7)$$

If the bin width is much larger than the dark matter momentum dispersion at any location, the expression above reduces to the familiar form [23]

$$\langle S_\nu \rangle = \frac{\Gamma_a}{4\pi\Delta\nu} \Theta(2\pi\Delta\nu - |\epsilon_0|) \int d\ell d\Omega B_{\nu_0} \rho_a e^{-\tau_{\nu_0}} , \quad (2.8)$$

where Θ is the Heaviside step function. We will use both the expressions above in obtaining our limits. In both cases, the signal needs then to be convolved with the detector energy response.

3 Data and Methods

3.1 Hubble Space Telescope (HST) Faint Object Spectrograph (FOS)

3.1.1 Data

We analyze blank sky observations acquired with the Hubble Space Telescope (HST) using the Faint Object Spectrograph (FOS) from February 1991 to March 1992, during

obs. ids	# Files	l [°]	b [°]	r_{min} [kpc]	D [10^{21} eV/cm ²]	Exp [s]
y0g11801t-y0g11803t	3	113.22	-66.76	8.12	1.832	450.00
y0g11901t-y0g11903t	3	304.72	-58.64	7.76	2.517	450.00
y0g11a01t-y0g11a03t	3	122.60	-73.74	8.12	1.837	450.00
y0g11b01t-y0g11b03t	3	301.92	-65.98	7.93	2.354	450.00
y0g11c01t-y0g11c03t	3	286.75	-75.99	8.10	2.113	450.00
y0g11d01t-y0g11d03t	3	284.24	-70.62	8.09	2.131	450.00
y0g11f01t-y0g11f03t	3	186.70	-59.04	8.12	1.522	450.00
y0g11l01t-y0g11l03t	3	179.61	-30.74	8.12	1.310	450.00
y0g11m01t-y0g11m03t	3	188.75	-36.57	8.12	1.345	450.00
y0g11o01t-y0g11o03t	3	278.25	-31.41	8.06	2.194	450.00
y0g11p01t-y0g11p03t	3	138.31	31.28	8.12	1.437	450.00
y0g11q01t-y0g11q03t	3	149.24	35.88	8.12	1.401	450.00
y0g11r01t-y0g11r03t	3	132.10	32.74	8.12	1.485	450.00
y0g11s01t-y0g11s0ct	6	129.61	31.50	8.12	1.499	899.99
y0g11t01t-y0g11t03t	3	207.74	45.72	8.12	1.450	450.00
y0g11u01t-y0g11u03t	3	171.04	49.88	8.12	1.438	450.00
y0g11v01t-y0g11v03t	3	238.71	40.54	8.12	1.610	450.00
y0g11w01t-y0g11w03t	3	238.59	41.12	8.12	1.612	450.00
y0g11x01t-y0g11x03t	3	239.26	41.22	8.12	1.619	450.00
y0g11y01t-y0g11y03t	3	238.95	41.53	8.12	1.617	450.00
y0g11z01t-y0g11z03t	3	192.59	53.21	8.12	1.472	450.00
y0g12001t-y0g12003t	3	232.14	50.78	8.12	1.616	450.00
y0g12101t-y0g12103t	3	180.63	62.67	8.12	1.560	435.00
y0g12201t-y0g12203t	3	167.50	80.09	8.12	1.819	450.00
y0g12401t-y0g12403t	3	285.89	75.63	8.10	2.111	435.00
y0g12501t-y0g12503t	3	97.37	86.57	8.12	2.006	450.00
y0g12602r-y0g12603r	2	120.19	46.45	8.12	1.650	375.00
y0g12801t-y0g12803t	3	148.17	78.80	8.12	1.822	450.00
y0g12901t-y0g12903t	3	117.11	45.26	8.12	1.672	450.00
y0g12b01t-y0g12b03t	3	110.99	53.17	8.12	1.771	450.00
y0g12c01t-y0g12c03t	3	18.61	68.68	7.62	2.627	450.00
y0g12d01t-y0g12d03t	3	337.83	48.84	6.44	3.519	450.00
y0g12e01t-y0g12e03t	3	351.74	56.93	6.84	3.220	450.00
y0g12g01t-y0g12g03t	3	7.36	41.14	5.40	4.381	450.00
y0g12h01t-y0g12h03t	3	7.23	41.02	5.39	4.394	450.00
y0g12i01t-y0g12i03t	3	94.76	42.04	8.12	1.939	450.00

Table 1: Summary of HST FOS data used in this work. The columns are: observation identifier, number of files for a given pointing of the telescope, galactic coordinates (l , b) of the pointing, distance of closest approach of the line of sight to the Galactic center r_{min} , D-factor obtained using the NFW of MilkyWayPotential2022 from the package `gala` [25], and exposure per energy bin (also called pixel).

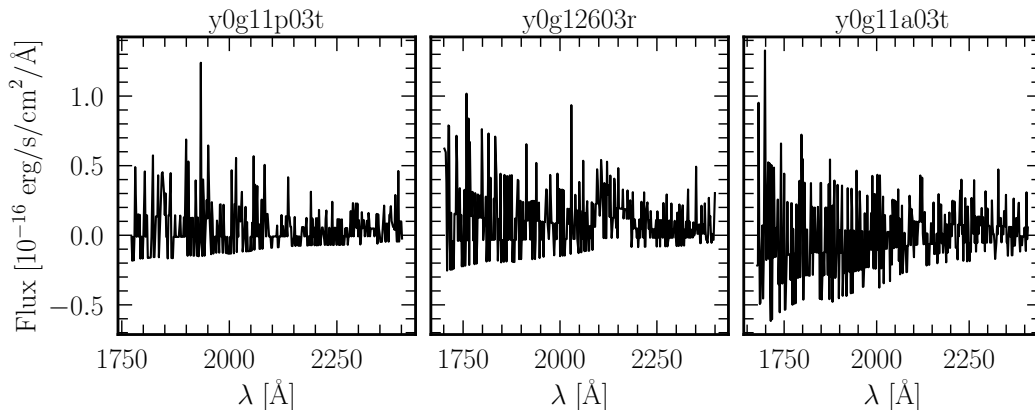


Figure 1: Three of the HST FOS spectra used in this work.

the science verification phase [11]. The goal of these observations was to study the sky background. Data were acquired under three proposal numbers: SV2965 (high galactic latitude), SV2966 (low galactic latitude), and SV2967 (low ecliptic latitude). Here we will use the high galactic latitude data set.

These data were acquired before the installation of the Corrective Optics Space Telescope Axial Replacement (COSTAR). COSTAR was introduced to correct the spherical aberration caused by a flaw in the HST primary mirror, affecting the FOS [26]. The aberration produced extended outer wings of the point spread function and consequent source acquisition failures, particularly in crowded fields, until COSTAR was deployed in 1994. However, the observations we use here targeted the diffuse sky background, and should therefore not be significantly affected by these aberration effects.

The FOS had two Digicon detectors: the blue detector (1150-5400 Å) and the red or amber detector (1620-8500 Å). The Digicons functioned by accelerating photoelectrons onto a linear array of 512 silicon diodes. The red detector was more sensitive than the blue one in the overlap region [26]. Additionally, we find that data from the blue detector are heavily contaminated by spurious spectral lines. For these reasons, our analysis focuses exclusively on the red-detector data. Moreover, we only use observations taken with the G160L grating, which is sensitive in the frequency range of our interest. This leaves us with 113 data files available on MAST [27] with 36 different pointings towards given galactic coordinates. The data are summarized in Table 1. In all but a couple of cases, there are three files for each pointing. The first file contains two exposures for a total of 300 seconds, the second, 5 exposures for a total of 600 seconds, and the third, 7 exposures for a total of 900 seconds. The exposure per energy bin (also called pixel) is given by the total exposure divided by 4, because the spectra were shifted in one-quarter diode increments, resulting in 2064 energy bins [26]. The lowest galactic latitude for observations in this set is $|\ell| = 30.7^\circ$ and the lowest distance of closest approach of any line of sight to the Galactic center is 5.39 kpc.

The target acquisition aperture (A-1 or 4.3) was used for all data. This aperture was a $4.3'' \times 4.3''$ square (pre-COSTAR). Since the height of a diode was $1.43''$, the effective collecting area was $4.3'' \times 1.43''$.

The spectral resolution is not a strong function of wavelength and can be derived from Tables 29.4 and 29.5 of [26]. With the G160L grating and 4.3 aperture, used for our data, we obtain a FWHM spectral resolution of 81 Å for extended sources filling the aperture, like the signal from ALP decay. Notice that no data taken high-dispersion gratings is available within SV2965.

Three example spectra are shown in Figure 1. We have removed energy bins flagged for data quality and wavelengths $\lambda < 1650$ Å, for which the red detector sensitivity drops. We do not perform any continuum subtraction.

3.1.2 Modeling of the signal

In order to bracket the uncertainty on our bound due to the dark matter energy density of the Milky Way, we consider several profiles. For our analysis, we take the Navarro-Frenk-White (NFW) profile [28]

$$\rho_a(r) = \frac{\rho_s}{\left(\frac{r}{r_s}\right) \left(1 + \frac{r}{r_s}\right)^2}, \quad (3.1)$$

from `MilkyWayPotential2022` from the galactic dynamics package `gala` [25], with parameters $\rho_s = 0.439$ GeV cm⁻³ and $r_s = 15.62$ kpc. In Eq. (3.1), ρ_s and r_s are the scale density and radius, respectively. This profile fits well various measurements of the MW enclosed mass up to galactic radii > 100 kpc, as well as measurements of the MW rotation curve between 5 and 20 kpc [29]. Notice that our results are completely insensitive to the structure of the Galactic DM halo within 5.39 kpc from its center. We further consider two profiles from [30]. Both models have been fitted to the Gaia rotation curve from [31] and the total MW mass from [32]. The first is best-fit NFW from [30] with parameters $\rho_s = 0.438$ GeV cm⁻³ and $r_s = 14.84$ kpc. The second is their best-fit contracted profile, derived by starting with an NFW with $\rho_s = 0.184$ GeV cm⁻³ and $r_s = 22.3$ kpc and applying a contraction due to the gravitational pull of baryons in the Galaxy located at the center of the halo. The functional shape of the contraction is informed by the structure formation simulations Auriga [33], APOSTLE [34, 35] and EAGLE [36]. The D-factors

$$D = \int_0^\infty dl \int d\Omega B(\Omega) \rho_a(r), \quad (3.2)$$

calculated assuming the `MilkyWayPotential2022` NFW profile, are listed in Table 1.

In order to allow comparison with works similar to ours, we consider three further NFW profiles. We will denote the results from these profiles as “extended analysis”. The first has $\rho_s = 0.256$ GeV cm⁻³ and $r_s = 19.1$ kpc. It is taken from the 2D 68% containment region for M_{200}^{DM} and c^{NFW} of [30] and was used in [37]. The second has $\rho_s = 0.184$ GeV cm⁻³ and $r_s = 24.42$ kpc. It is from [38] and was used in [14, 15]. The third and final profile, taken from [39], was used in [40] and has $\rho_s = 0.566$ GeV cm⁻³ and $r_s = 14.46$ kpc.

Throughout, we use a distance of the Sun from the Galactic center of $R = 8.122$ kpc [41] and the Galactic extinction law from Ref. [42] with magnitude along the

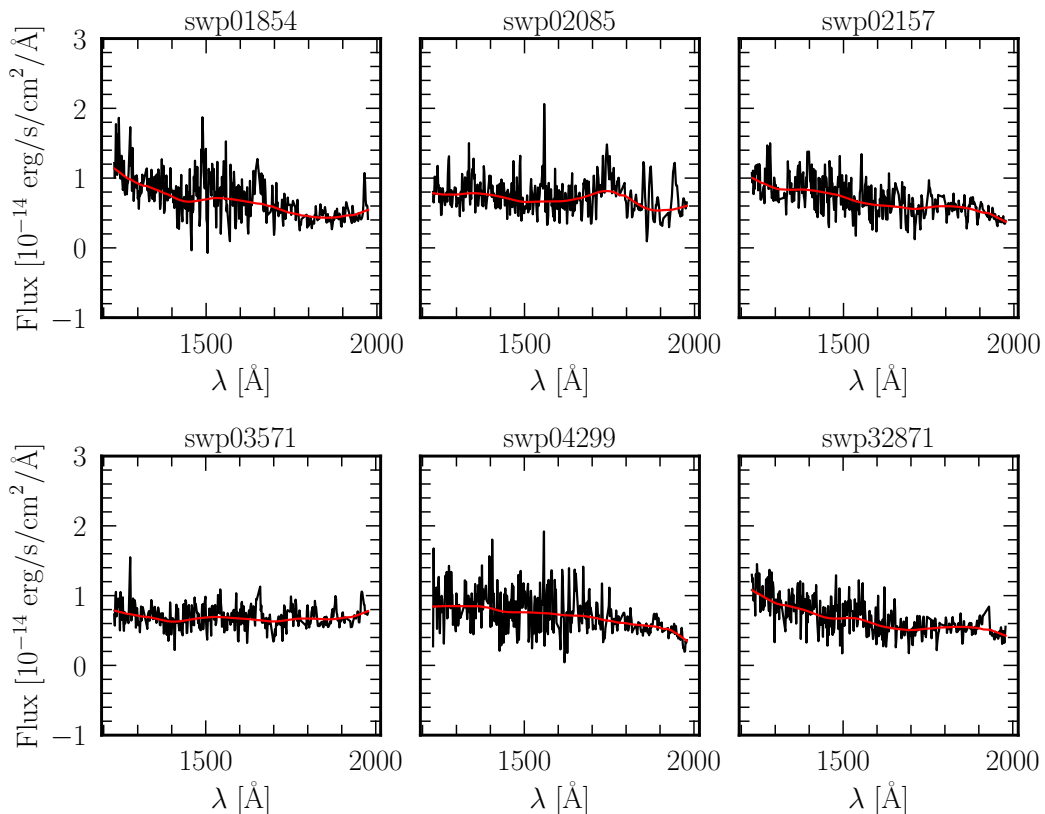


Figure 2: IUE spectra acquired with the short-wavelength spectrograph. Red lines mark the continuum model.

line of sight from [43]. We conservatively apply the suppression of the flux from dust extinction as if all emission originated at infinity. We use Eq. (2.8) to compute the signal since the spectral resolution is much larger than the signal’s intrinsic bandwidth.

3.2 International Ultraviolet Explorer (IUE)

3.2.1 Data

We analyze all International Ultraviolet Explorer (IUE) data with pointing within one arcminute of M87 available on the IUE Newly Extracted Spectra (INES) system [44]. We find six spectra collected with the short wavelength spectrograph (1150-2000 Å), and five spectra collected with the low-wavelength spectrograph (1850-3300 Å), one with the prime and five with the redundant camera. All considered data are taken in the low-dispersion mode and through the large apertures.

The INES system was created to address concerns [44, 45] regarding the calibration of low-dispersion spectra in the New Spectroscopic Image Processing System (NEWSIPS) [46]. In particular, the INES system takes the bi-dimensional, spatially resolved, rotated images (SILO files) created by NEWSIPS, and extracts one-dimensional spectra, applying improved noise models, background determination, and extraction profile. Two additional spectra with pointing within 1’ of M87 are available

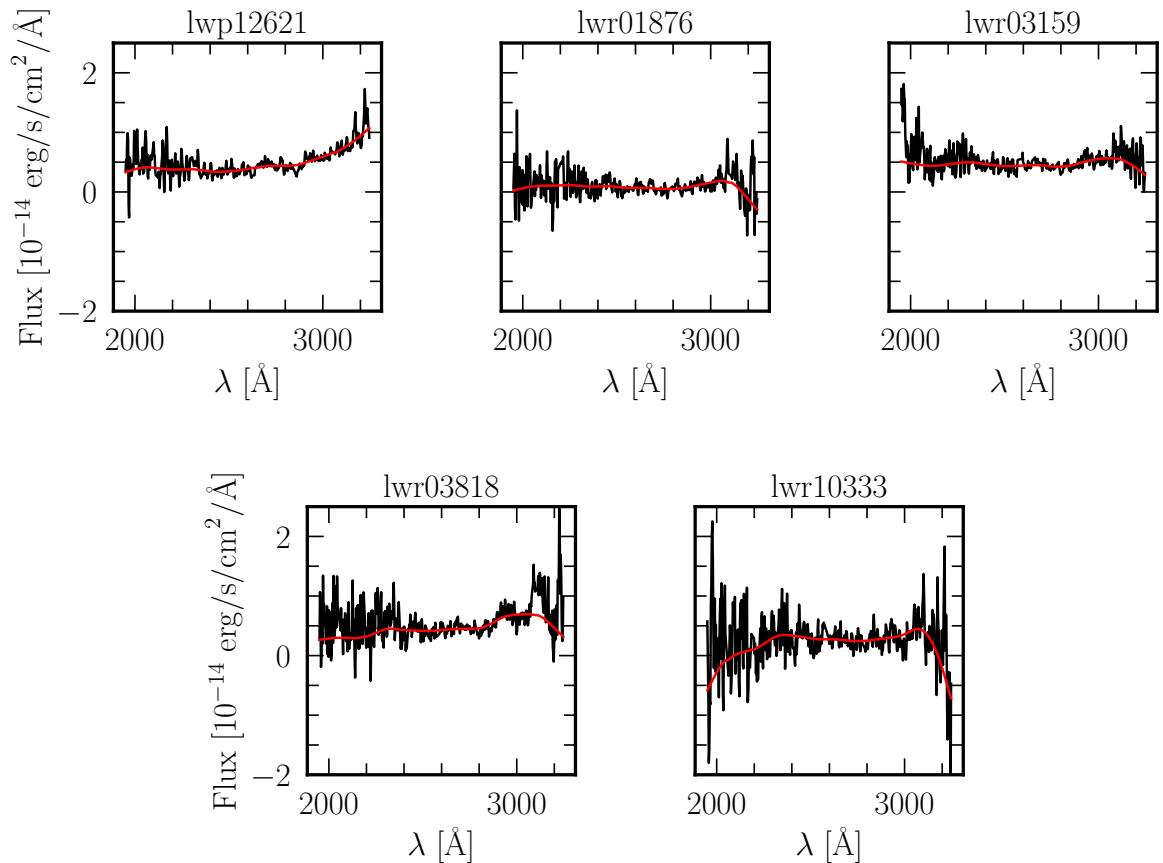


Figure 3: IUE spectra acquired with the long-wavelength spectrograph. Red lines mark the continuum model.

obs. id	exposure [ks]	ang. sep. [']	ang. sep. M87 [']	\tilde{D} [10^{24} eV/cm 2]
lwp12621	21.18	0.553	0.079	1.51
lwr01876	20.40	0.510	0.165	1.49
lwr03159	23.40	0.510	0.165	1.49
lwr03818	13.80	0.416	0.144	1.57
lwr10333	3.60	0.542	0.087	1.46
swp01854	18.00	0.564	0.037	1.48
swp02085	22.98	0.510	0.165	1.53
swp02157	24.00	0.601	0.109	1.46
swp03571	22.20	0.510	0.165	1.53
swp04299	25.80	0.416	0.144	1.62
swp32871	44.88	0.495	0.156	1.55

Table 2: IUE observations used in this work. The columns are: the observation identifier, the total exposure, the angular separation from our reference center and from the center of M87, and the modified D-factor \tilde{D} defined in Eq. (3.3), calculated using the parameters of our fiducial analysis.

on MAST [27]. However, since they were calibrated with NEWSIPS and not with INES, we do not include them in our analysis.

The sizes of the large apertures as projected on the cameras are reported in [47] (Section 2.2). IUE large apertures are slots, with a size of approximately 10 by 20 arcsec. In the following, we will approximate them as circles with radius $R = \sqrt{A/\pi}$, where A is the area given in [47]. The impact of this approximation on our bounds is subdominant compared to other sources of systematic errors that we account for.

The spectral resolution of IUE’s spectrographs is approximately 6 Å. We take the FWHM resolution along the dispersion direction from Figure 2.19 of [47], interpolating linearly between data points. In creating the SILO files, NEWSIPS applies a de-tilting of the 2D image if the source is classified as extended, i.e. filling the aperture [46]. This adjustment is necessary because the large aperture’s major axis is not aligned perpendicularly to the dispersion direction. Extracting the 1D spectrum of an extended source without de-tilting—by simply summing the flux perpendicular to the dispersion—results in a degradation of the spectral resolution of 20 to 25%. De-tilting is not necessary for point sources that are localized within the aperture. The emission from the decay of ALP dark matter we search for here is an extended source. However, some of the spectra we consider were extracted as point sources. For those, we multiply the FWHM spectral resolution from Figure 2.19 of [47] by a factor 1.25.

The spectra are shown in Figures 2 and 3 and listed in Table 2, along with the exposure, angular separation from the center of the DM halo used for our fiducial analysis and from M87, and modified D-factor (see Section 3.2.2). We remove energy bins flagged for data quality as well as region $\lambda < 1230$ Å, to remove the bright Ly α emission. For long-wavelength spectrograph data, we restrict the range to $1950 \text{ \AA} < \lambda < 3250 \text{ \AA}$. The red lines in Figures 2 and 3 mark the continuum model that we subtract from the data. For our search, further background subtraction is appropriate in addition to what is already done in INES. While INES accounts for instrumental backgrounds such as radioactive decay, sky background, scattered light, and readout noise, in our case, continuum emission from the target of observation (M87) also constitutes a background. To determine the continuum level, we use the asymmetrically reweighted Penalized Least Squares algorithm (arPLS) [48] with a smoothness parameter of 10^5 .

3.2.2 Modeling of the signal

For our fiducial analysis, we adopt the DM profile for the Virgo dark halo from [49]. It is an NFW profile with scale density $\rho_s = 3.2 \times 10^5 M_\odot \text{ kpc}^{-3}$ and scale radius $r_s = 560 \text{ kpc}$. We adopt a distance $d = 15.9 \text{ Mpc}$ to the center of the Virgo cluster [50] and a redshift $z = 0.0038$. Finally, we choose the reference center of the DM halo of Virgo from [51], with galactic coordinates $l = 283.7606^\circ$ and $b = +74.4835^\circ$.

To estimate the systematic uncertainty on our bound due to modeling of the DM halo, we vary ρ_s and r_s within the error bars reported in [49]: $\rho_s = (3.2^{+2.6}_{-1.3}) \times 10^5 M_\odot \text{ kpc}^{-3}$ and $r_s = 560^{+150}_{-200} \text{ kpc}$. We also consider two additional estimates of the distance to the center of Virgo, $d = 16.5 \text{ Mpc}$ from [52] and $d = 15.46 \text{ Mpc}$ from [53]. Finally, we explore the uncertainty due to the position of the center of the DM halo. From Figure 4, it’s clear that assuming the center of the DM halo to coincide with

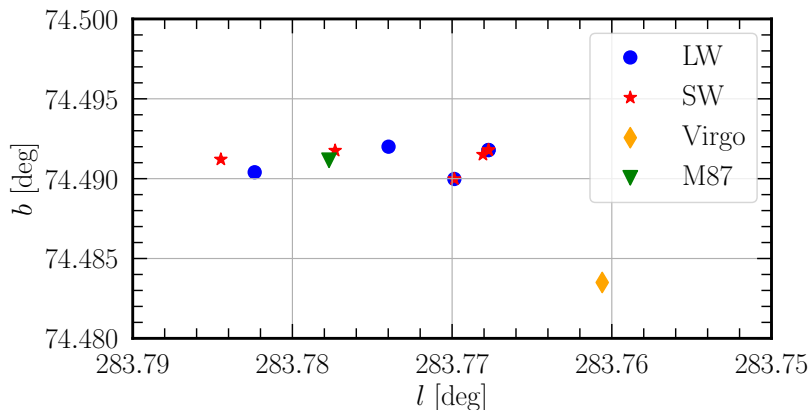


Figure 4: Galactic coordinates of the observations taken with the short (red stars) and long (blue dots) wave-length spectrographs. The green triangle marks the position of M87, while the orange diamond is the assumed position of the center of the Virgo DM halo for our fiducial analysis.

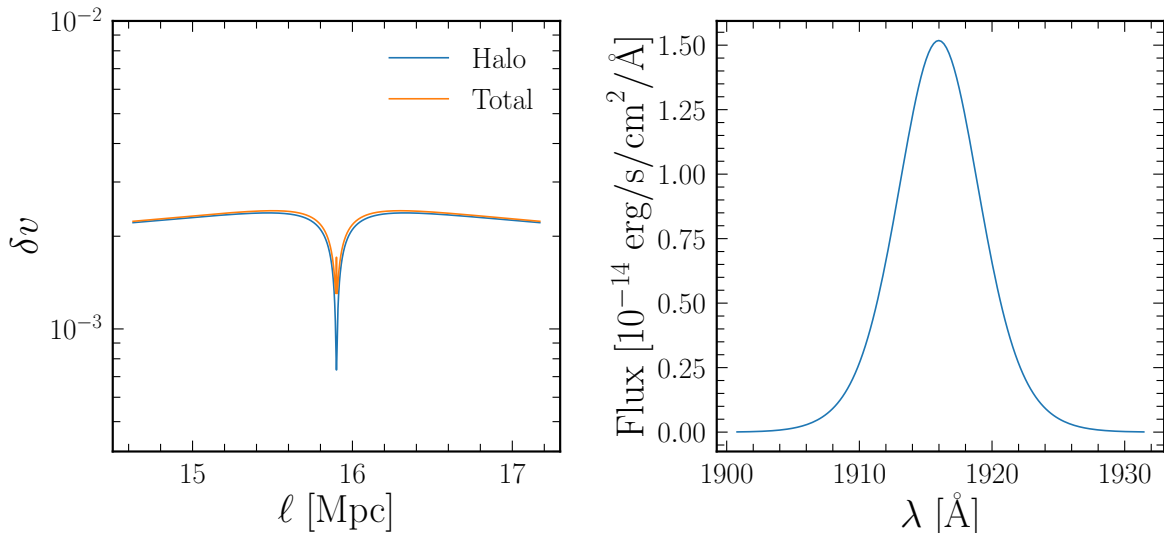


Figure 5: Left: Velocity dispersion as a function of the distance along the line of sight ℓ , for a line of sight passing through the center of the swp01854 observation. The orange line shows the total velocity dispersion, given by the halo contribution (blue line) plus the BH contribution. **Right:** Expected signal for observation swp01854, $m_a = 13$ eV and $g_{a\gamma} = 10^{-12}$ GeV $^{-1}$, assuming the modeling of our fiducial analysis.

M87, whose position we take from [54], will yield a more stringent bound than our fiducial analysis since observations are focused there. The angular separation between M87 and our reference center is about $30''$, corresponding to a projected distance of about 2.5 kpc. To bracket the uncertainty on our bound, we will consider the case in which the center of the halo coincides with M87, and the case in which the center is $30''$ away from our reference center in the direction opposite to M87.

We compute the velocity dispersion $\delta v(r)$ integrating the spherically symmetric Jeans equation assuming no velocity anisotropy (see for example Ref. [55]). We consider an additional component of the velocity dispersion around the supermassive black hole (BH) M87*, $\delta v_{BH} = \sqrt{2GM_{BH}/r}$, where $M_{BH} = 6.5 \times 10^9 M_\odot$ [56] and r is the distance from the BH position. We conservatively assume that the distance to the BH is the same as the distance to the center of the DM halo¹. The left panel of Figure 5 shows the velocity dispersion along the line of sight to the center of the swp01854 observation. The component due to the halo is consistent with measurements of the velocity dispersion [49, 57] of order 640 km/s.

For each spectrum, Table 2 reports the angular separation from the reference center of the DM halo and from M87, and modified D-factor

$$\tilde{D} = \langle \delta v \rangle \int_0^\infty dl \int d\Omega B(\Omega) \frac{\rho_a}{\delta v} \quad \langle \delta v \rangle = \frac{1}{V} \int_{d-r_s}^{d+r_s} dl \int d\Omega B(\Omega) \delta v, \quad (3.3)$$

where V is the volume of the integration region. The D-factor due to the MW halo along the same line of sight is typically a factor of 20 smaller than that due to Virgo.

We apply the dust extinction in the Virgo intra-cluster medium from [58], with an extinction $A_V = 0.14$ mag and a Magellanic Cloud-like extinction law [59], i.e. with the shape functional shape of [42] and $R_V = 3.41$. Galactic extinction is modeled in the same way as for HST data. The expected signal for swp01854, with an ALP mass of 13 eV and coupling $g_{a\gamma} = 10^{-12} \text{ GeV}^{-1}$, is shown on the right panel of Fig. 5. It has a FWHM of about 7.3 Å, comparable to IUE's spectral resolution. We then compute the flux density as in Eq. (2.7) and convolve it with the detector response, which we take to be a Gaussian with a standard deviation $\sigma_\lambda = \text{FWHM}/(2\sqrt{2\log(2)})$ and FWHM from [47].

4 Results

We extract our limits using a Gaussian likelihood for each data set

$$\mathcal{L}_j = e^{-\chi_j^2/2} \quad \text{with} \quad \chi_j^2 = \sum_{i=1}^{N_{bin}} \left(\frac{S_{th}^i - S_{obs}^i}{\sigma_i} \right)^2, \quad (4.1)$$

where i runs over the energy bins, S_{th}^i is the theoretical estimate for the flux density, S_{obs}^i is the observed flux density (minus the continuum emission determined by the arPLS algorithm for IUE data), and σ_i is the statistical error. We combine different data sets, labeled by j , by multiplying the respective likelihoods

$$\mathcal{L}(g_{a\gamma}) = \prod_j \mathcal{L}_j(g_{a\gamma}) \quad \text{i.e.,} \quad \chi^2(g_{a\gamma}) = \sum_j \chi_j^2(g_{a\gamma}). \quad (4.2)$$

We set bounds using the test statistics defined as $\lambda_c(g_{a\gamma}) = -2 \ln[\mathcal{L}(g_{a\gamma})/\mathcal{L}(g_{a\gamma}^{b.f.})]$ for $g_{a\gamma} \geq g_{a\gamma}^{b.f.}$ and $\lambda_c(g_{a\gamma}) = 0$ for $g_{a\gamma} < g_{a\gamma}^{b.f.}$, where $g_{a\gamma}^{b.f.}$ is the value of the coupling

¹This choice implies that the large velocity dispersion around the black hole suppresses the contribution the NFW cusp to \tilde{D} .

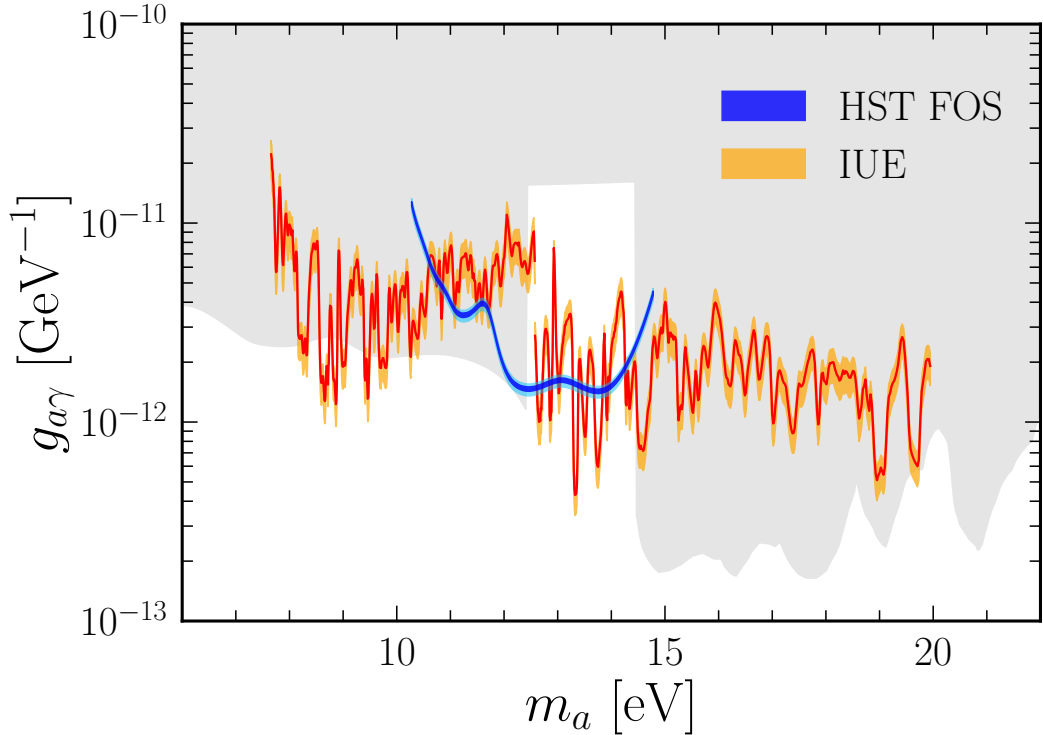


Figure 6: 95% C.L. upper bounds obtained from HST FOS (red/orange) and IUE (blue) data. The thickness of the colored bands accounts for systematic errors due to the modeling of the signal. The dark gray shaded regions show existing bounds from evolution in globular clusters [60], while the region in light gray is excluded by Refs. [18, 19, 21, 61–63].

that maximizes the likelihood at fixed ALP mass. We assume $\lambda_c(g_{a\gamma})$ follows a half χ^2 distribution with one degree of freedom [64], and set 95% C.L. bounds on $g_{a\gamma}$, by requiring $\chi^2 = \chi_{b.f.}^2 + 2.71$, where $\chi_{b.f.}^2$ is the χ^2 of the best-fit model.

4.1 HST FOS

The 95% C.L. upper bound derived from the HST FOS data are shown in Figure 6 by the dark blue band. The average value of the bound in the mass range 12.4 to 14.5 eV is $1.6 \times 10^{-12} \text{ GeV}^{-1}$.

The three DM profiles considered yield bounds within 5% of each other, with the `MilkyWayPotential2022` NFW being the most optimistic and the best-fit NFW from [30] being the most conservative. We show the results of our extended analysis with a light blue band. We find that the model from [40] is the most optimistic, while that from [37] is the more conservative. These models yield bounds within 14% of each other. Using an alternative Galactic extinction law from [65] improves our bound by a factor of 0.75%

4.2 IUE

Our 95% C.L. upper bound is shown as a red line in Figure 6, while the orange band indicates the systematic uncertainty due to the modeling of Virgo’s DM halo. The lower boundary of the band is obtained assuming the most optimistic dark matter profile (largest ρ_s and smallest r_s) from [49] and that the center of the halo coincides with M87. The upper boundary is obtained with the most pessimistic profile from [49] and assuming the center of the halo is 0.5’ away from our reference center in the direction opposite to M87.

Averaging over ALP masses, the bounds fluctuate by +8.5% and -11% compared to the fiducial analysis, with the halo profile and center position contributing variations of +4.1% and -5.0%, and 4.3% and -6.0%, respectively, when considered separately. We find that changing the distance to the center of the halo does not affect the bound in any significant way. We further test how our bounds change when we use a constant velocity dispersion of 640 km/s and find a modest weakening of the bounds by 2%. Considering a different Galactic extinction law from [65] worsens the bounds by less than 0.5%.

Finally, another source of systematic uncertainty is the continuum model. We check how setting the smoothness parameter λ of the arPLS algorithm to 10^3 or 10^7 affects our bounds. Either choice can strengthen or loosen the bound for a given ALP mass. On average the bounds worsen by less than 2% compared to the fiducial case $\lambda = 10^5$ for short wavelength spectra, while they fluctuate by +5.2% and - 1.7% for long wavelength spectra.

5 Comparison with other work

Reference [22] reports strong bounds in an ALP mass range overlapping with ours, based on data from [56]. Here we revisit those constraints.

In April 2018, a coordinated multi-wavelength campaign involving over two dozen observatories, including the Event Horizon Telescope (EHT), observed the supermassive black hole M87*, capturing data from radio to very high-energy gamma-rays. The relevant data points for us are those acquired with Swift-UVOT (6 data points) and AstroSat-UVIT (1 data point). These data are listed in Table 1 of [22], which is in turn taken from Table C.1 of [56]. Swift-UVOT observed M87 in its optical (v , b and u) and UV ($w1$, $m2$ and $w2$) photometric bands. The central frequencies and bandwidths of Swift-UVOT can be found in Table 1 of Ref. [66]. The resolution $\Delta\lambda/\lambda$ ranges from 0.14 to 0.34, much larger than the DM velocity dispersion. The AstroSat-UVIT datapoint is obtained with the BaF2 filter, with a $\Delta\lambda/\lambda$ of about 0.25.

In the spirit of comparing with [22], we adopt the same dark matter profile. We assume an NFW profile for the Virgo dark matter halo with $\rho_s = 6.96 \times 10^5 M_\odot/\text{kpc}^{-3}$, $r_s = 403.8$ kpc, and a distance of 17.2 Mpc [67]. We take the center of the halo to coincide with the position of M87* and assume that the observations are centered there. We remove a region of 100 Schwarzschild radii around the BH.

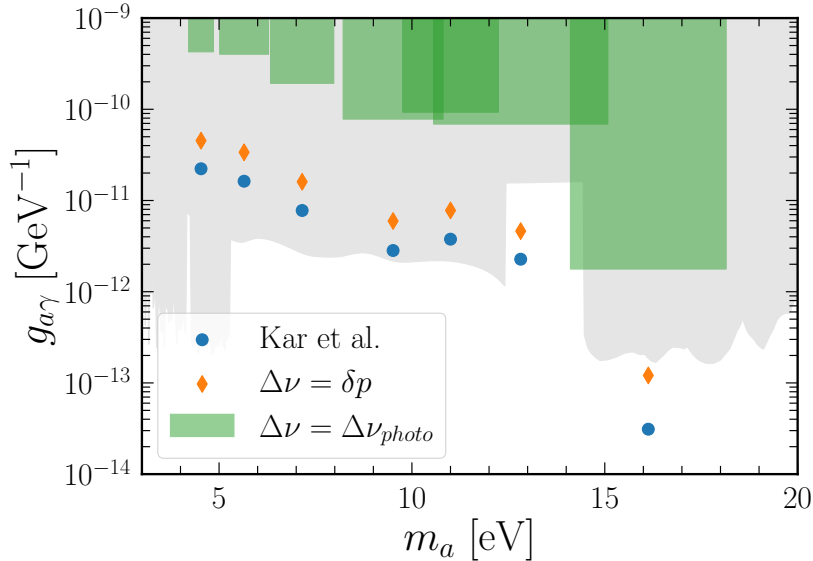


Figure 7: Constraints on the ALP–photon coupling $g_{a\gamma}$ as a function of ALP mass from Swift-UVOT and AstroSat-UVIT observations of M87 (green bands). Blue dots reproduce the bounds of [22], while orange diamonds are obtained correcting for aperture interpretation and flux density definition. Green bands show the correct bounds when accounting for the finite photometric bandwidth, which significantly weakens sensitivity to the narrow spectral line expected from ALP decay. The width of the green bands represents the width of Swift-UVOT and AstroSat-UVIT photometric bands.

First, we reproduce the results of [22]. To calculate the flux from ALP decay, we use their Eq. (2.3)

$$\langle S_\nu \rangle = \Gamma_a \int d\ell d\Omega B(\Omega) \frac{\rho_a}{\delta p} = \frac{\Gamma_a}{\langle \delta p \rangle} \tilde{D} . \quad (5.1)$$

Here, the velocity dispersion $\delta v = \delta p/m_a$ has two components: a halo component set to 10^{-3} , and a black hole component as described in Section 3.

With this setup, we are able to accurately reproduce the bounds obtained with the “conservative approach” of [22]. This approach consists in requiring that the flux density from ALP decay does not exceed the measured one. We match their results by assuming: 1) top-hat circular apertures with a radius of $3''$ for Swift-UVOT and of $300''$ for AstroSat-UVIT, 2) measured flux density obtained by dividing νS_ν reported in Table 1 of [22] (or Table C.1 of [56]) by the central frequency of the respective frequency band.

From Table C.1 of [56], we see however that $3''$ and $300''$ are the FWHM angular extents over which the flux is collected. If these values are interpreted as diameters, rather than radii, of the apertures, we obtain the modified D-factors $\tilde{D} = 6.2 \times 10^{22} \text{ eV/cm}^2$ for the $3''$ aperture and $\tilde{D} = 3.7 \times 10^{26} \text{ eV/cm}^2$ for the $300''$ one. These modified D-factors are a factor of 3.9 and 3.3 smaller than those resulting from taking $3''$ and $300''$ as radii. Additionally, for the AstroSat-UVIT observation, the flux

density in the sixth column of Table C.1 of [56] corresponds not to νS_ν , divided by the central frequency, but by the bandwidth. Taking into account the correct \tilde{D} and taking the observed flux density from the sixth column of Table C.1 of [56], we obtain the bounds shown in Fig. 7 as orange diamonds. These are a factor of 2 and 4 weaker for Swift and AstroSat, respectively, than reported in [22].

We now address the central issue: Eq. (5.1) is not the correct expression to compute the flux in a photometric band that is significantly broader than the intrinsic bandwidth of the ALP signal. Instead, one should use Eq. (2.8)², with $\Delta\nu = \Delta\nu_{photo}$, the bandwidth of the photometric filter, because this is the frequency range over which the ALP signal gets averaged. The bounds obtained this way are shown in Fig 7 as green bands. They are weaker by factors of 10–15 compared to the orange diamonds, leading to a total weakening of a factor of 20–30 for Swift and about 60 for AstroSat, relative to the original bounds of [22]. Additional weakening may come from assuming a different center and profile of the dark halo, as discussed in Section 3.2.

Lastly, we comment on the bound obtained in [22] from “historical data” consisting of six data points. In the UV region, these bounds are obtained from IUE data, presumably from rebinning the spectra used in Ref. [68]. That study focused on emission from the nucleus and jet of M87 using four IUE spectra—specifically, swp03571, swp04299, lwr3159, and lwr03818—which are also part of the dataset we analyzed in Section 3.2. Our bounds are based on these and additional observations analyzed at full spectral resolution. As a result, our limits are likely to be more stringent than what can be obtained from rebinning a smaller set of the data.

6 Conclusions

In this work, we searched for a spectral line from the decay of axion-like particle (ALP) dark matter in ultraviolet data from the Hubble Space Telescope (HST) and the International Ultraviolet Explorer (IUE). We focused on the 12.4–14.5 eV ALP mass range, which remains relatively unexplored and is within the sensitivity window of these instruments.

Using archival blank-sky data from the HST Faint Object Spectrograph (FOS) and observations of M87 from IUE, we derived new upper bounds on the ALP–photon coupling $g_{a\gamma}$. Our most stringent limit, obtained from HST, excludes values of $g_{a\gamma}$ above $1.6 \times 10^{-12} \text{ GeV}^{-1}$, or ALP lifetimes below $2 \times 10^{25} \text{ s}$, and improves upon previous constraints by an order of magnitude. IUE data from observations toward the Virgo cluster yield complementary bounds at the level of $2.1 \times 10^{-11} \text{ GeV}^{-1}$. Although the HST FOS had better sensitivity than the IUE spectrographs, the bounds obtained with the two instruments are comparable due to the lower D-factor of the Milky Way compared to Virgo and to the poorer spectral resolution of the low-dispersion configurations of the FOS. The narrower instrumental response of IUE better matches the intrinsic width of the ALP decay line, leading to a more favorable signal-to-noise ratio despite lower sensitivity.

²We do not include extinction or the frequency dependence of the beam.

We also revisited recent claims in the literature based on photometric data from Swift-UVOT and AstroSat-UVIT. We showed that these bounds are significantly over-estimated due to incorrect treatment of the ALP spectral line width relative to the broad instrumental bands. When properly accounting for spectral resolution, we find the resulting constraints are weakened by well over one order of magnitude.

Our analysis demonstrates the power of spectroscopic data for probing ALP dark matter in the extreme ultraviolet and highlights the importance of accurate spectral modeling. Future UV observatories with improved sensitivity may further extend the reach of this method into new regions of parameter space.

Acknowledgements

ET is grateful to Marco Regis, Anne Green, and Alfonso Aragon-Salamanca for useful discussions. ET is supported by STFC Consolidated Grant [ST/T000732/1]. This article/publication is based upon work from COST Action COSMIC WISPerS CA21106, supported by COST (European Cooperation in Science and Technology)”.

Data Availability Statement: The data used in this work is publicly available from the Mikulski Archive for Space Telescopes (MAST) [27] or the IUE Newly Extracted Spectra (INES) system [69].

References

- [1] P. Arias, D. Cadamuro, M. Goodsell, J. Jaeckel, J. Redondo, et al., *WISPy Cold Dark Matter*, *JCAP* **06** (2012) 013, [[1201.5902](#)].
- [2] R. D. Peccei and H. R. Quinn, *CP Conservation in the Presence of Instantons*, *Phys. Rev. Lett.* **38** (1977) 1440–1443. [[328\(1977\)](#)].
- [3] R. D. Peccei and H. R. Quinn, *Constraints Imposed by CP Conservation in the Presence of Instantons*, *Phys. Rev.* **D16** (1977) 1791–1797.
- [4] S. Weinberg, *A New Light Boson?*, *Phys. Rev. Lett.* **40** (1978) 223–226.
- [5] F. Wilczek, *Problem of Strong p and t Invariance in the Presence of Instantons*, *Phys. Rev. Lett.* **40** (1978) 279–282.
- [6] M. Dine and W. Fischler, *The Not So Harmless Axion*, *Phys. Lett.* **B120** (1983) 137–141. [[URL\(1982\)](#)].
- [7] L. F. Abbott and P. Sikivie, *A Cosmological Bound on the Invisible Axion*, *Phys. Lett.* **B120** (1983) 133–136. [[URL\(1982\)](#)].
- [8] J. Preskill, M. B. Wise, and F. Wilczek, *Cosmology of the Invisible Axion*, *Phys. Lett.* **B120** (1983) 127–132. [[URL\(1982\)](#)].
- [9] J. N. Bahcall, S. Kirhakos, D. H. Saxe, and D. P. Schneider, *The hubble space telescope: A new tool for astronomy*, *Science* **254** (1991), no. 5029 46–53.
- [10] A. Boggess, F. A. Carr, D. C. Evans, and et al., *The international ultraviolet explorer: A space telescope for ultraviolet astronomy*, *Nature* **275** (1978) 372–377.

- [11] R. W. Lyons, W. A. Baity, E. A. Beaver, R. D. Cohen, V. T. Junkkarinen, et al., *On-orbit sky background measurements with the fos*, in *Space Astronomical Telescopes and Instruments II, Proceedings of SPIE*, vol. 1945, (Orlando, FL, USA), Society of Photo-Optical Instrumentation Engineers, Apr., 1993. NASA CR-204004.
- [12] W. Yin and K. Hayashi, *Indirect Detection of Decaying Dark Matter with High Angular Resolution: Case for axion search by IRCS at Subaru Telescope*, [2305.13415](#).
- [13] R. Janish and E. Pinetti, *Hunting Dark Matter Lines in the Infrared Background with the James Webb Space Telescope*, [2310.15395](#).
- [14] E. Pinetti, *First constraints on QCD axion dark matter using James Webb Space Telescope observations*, [2503.11753](#).
- [15] A. K. Saha, S. Bouri, A. Das, A. Dubey, and R. Laha, *Shedding Infrared Light on QCD Axion and ALP Dark Matter with JWST*, [2503.14582](#).
- [16] D. Grin, G. Covone, J.-P. Kneib, M. Kamionkowski, A. Blain, et al., *A Telescope Search for Decaying Relic Axions*, *Phys. Rev. D* **75** (2007) 105018, [[astro-ph/0611502](#)].
- [17] E. Todarello, M. Regis, J. Reynoso-Cordova, M. Taoso, D. Vaz, et al., *Robust bounds on ALP dark matter from dwarf spheroidal galaxies in the optical MUSE-Faint survey*, *JCAP* **05** (2024) 043, [[2307.07403](#)].
- [18] H. Wang et al., *Spectroscopic search for optical emission lines from dark matter decay*, *Phys. Rev. D* **110** (2024), no. 10 103007, [[2311.05476](#)].
- [19] E. Todarello and M. Regis, *Bounds on axions-like particles shining in the ultra-violet*, *JCAP* **05** (2025) 070, [[2412.02543](#)].
- [20] K. Nakayama and W. Yin, *Anisotropic cosmic optical background bound for decaying dark matter in light of the LORRI anomaly*, *Phys. Rev. D* **106** (2022), no. 10 103505, [[2205.01079](#)].
- [21] P. Carena, G. Lucente, and E. Vitagliano, *Probing the blue axion with cosmic optical background anisotropies*, *Phys. Rev. D* **107** (2023), no. 8 083032, [[2301.06560](#)].
- [22] A. Kar, S. Roy, and P. Sarkar, *Constraining eV-scale axion-like particle dark matter: insights from the M87 Galaxy*, . [[2501.01860v2](#)].
- [23] A. Caputo, M. Regis, M. Taoso, and S. J. Witte, *Detecting the Stimulated Decay of Axions at RadioFrequencies*, *JCAP* **1903** (2019), no. 03 027, [[1811.08436](#)].
- [24] E. Todarello, F. Calore, and M. Regis, *Anatomy of astrophysical echoes from axion dark matter*, *JCAP* **05** (2024) 040, [[2311.00051](#)].
- [25] A. M. Price-Whelan, *Gala: A Python package for galactic dynamics*, *The Journal of Open Source Software* **2** (Oct., 2017) 388.
- [26] C. Keyes, S. Heap, D. Lindler, D. Sahnou, M. Rosa, et al., *Faint Object Spectrograph Instrument Handbook, Version 7.0*. Space Telescope Science Institute, Baltimore, MD, 1998. https://www.stsci.edu/files/live/sites/www/files/home/hst/documentation/_documents/fos/FOS-DHB-1998.pdf.
- [27] “Mikulski Archive for Space Telescopes (MAST).” <https://mast.stsci.edu/search/ui/#/>. Accessed: 2025-06-20.

- [28] J. F. Navarro, C. S. Frenk, and S. D. M. White, *The Structure of cold dark matter halos*, *Astrophys. J.* **462** (1996) 563–575, [[astro-ph/9508025](#)].
- [29] J. A. S. Hunt and E. Vasiliev, *Milky Way dynamics in light of Gaia*, *New Astron. Rev.* **100** (June, 2025) 101721, [[2501.04075](#)].
- [30] M. Cautun, A. Benítez-Llambay, A. J. Deason, C. S. Frenk, A. Fattahi, et al., *The milky way total mass profile as inferred from Gaia DR2*, *MNRAS* **494** (May, 2020) 4291–4313, [[1911.04557](#)].
- [31] A.-C. Eilers, D. W. Hogg, H.-W. Rix, and M. K. Ness, *The Circular Velocity Curve of the Milky Way from 5 to 25 kpc*, *ApJ* **871** (Jan., 2019) 120, [[1810.09466](#)].
- [32] T. M. Callingham, M. Cautun, A. J. Deason, C. S. Frenk, W. Wang, et al., *The mass of the Milky Way from satellite dynamics*, *MNRAS* **484** (Apr., 2019) 5453–5467, [[1808.10456](#)].
- [33] R. J. J. Grand et al., *The Auriga Project: the properties and formation mechanisms of disc galaxies across cosmic time*, *MNRAS* **467** (2017) 179.
- [34] A. Fattahi et al., *The APOSTLE simulations: solutions to the Local Group’s cosmic puzzles*, *MNRAS* **457** (2016) 844.
- [35] T. Sawala et al., *The APOSTLE simulations: galaxies in the Local Group*, *MNRAS* **457** (2016) 1931.
- [36] J. Schaye et al., *The EAGLE project: simulating the evolution and assembly of galaxies and their environments*, *MNRAS* **446** (2015) 521.
- [37] S. Roy, C. Blanco, C. Dessert, A. Prabhu, and T. Temim, *Sensitivity of JWST to eV-Scale Decaying Axion Dark Matter*, *Phys. Rev. Lett.* **134** (2025), no. 7 071003, [[2311.04987](#)].
- [38] M. Cirelli, G. Corcella, A. Hektor, G. Hutsi, M. Kadastik, et al., *PPPC 4 DM ID: A Poor Particle Physicist Cookbook for Dark Matter Indirect Detection*, *JCAP* **1103** (2011) 051, [[1012.4515](#)]. [Erratum: *JCAP*1210,E01(2012)].
- [39] M. Cirelli, A. Strumia, and J. Zupan, *Dark Matter*, [2406.01705](#).
- [40] M. Regis, M. Taoso, and J. Terol Calvo, *Searching for axion-like particles with SPHEREx*, *JCAP* **05** (2025) 008, [[2412.12286](#)].
- [41] GRAVITY Collaboration, R. Abuter, A. Amorim, N. Anugu, M. Bauböck, et al., *Detection of the gravitational redshift in the orbit of the star S2 near the Galactic centre massive black hole*, *A&A* **615** (July, 2018) L15, [[1807.09409](#)].
- [42] J. A. Cardelli, G. C. Clayton, and J. S. Mathis, *The Relationship between Infrared, Optical, and Ultraviolet Extinction*, *ApJ* **345** (Oct., 1989) 245.
- [43] NASA/IPAC, *Galactic Dust Reddening and Extinction Service*, 2013.
- [44] P. M. Rodríguez-Pascual, R. González-Riestra, N. Schartel, and W. Wamsteker, *Improved data extraction procedures for iue low resolution spectra: the ines system*, [astro-ph/9907151](#).
- [45] D. Massa and E. L. Fitzpatrick, *A recalibration of iue newsips low dispersion data*, *Astrophys. J. Suppl.* **126** (2000) 517–536, [[astro-ph/9812152](#)].

- [46] J. S. Nichols and J. L. Linsky, *The Final Archive and Recalibration of the International Ultraviolet Explorer (IUE) Satellite*, *AJ* **111** (Jan., 1996) 517.
- [47] M. P. Garhart, M. A. Smith, B. E. Turnrose, K. L. Levay, and R. W. Thompson, *International Ultraviolet Explorer New Spectral Image Processing System Information Manual: Version 2.0, IUE NASA Newsletter* **57** (Oct., 1997) 1–267.
- [48] S.-J. Baek, A. Park, Y.-J. Ahn, and J. Choo, *Baseline correction using asymmetrically reweighted penalized least squares smoothing*, *The Analyst* **140** (Jan., 2015) 250–257.
- [49] D. E. McLaughlin, *Evidence in Virgo for the Universal Dark Matter Halo*, *Astrophys. J. Lett.* **512** (1999) L9, [[astro-ph/9812242](#)].
- [50] R. B. Tully, H. M. Courtois, and J. G. Sorce, *Cosmicflows-3*, *Astron. J.* **152** (2016) 50, [[1605.01765](#)].
- [51] S. Sazonov et al., *SRG/ART-XC all-sky X-ray survey: Catalog of sources detected during the first five surveys*, *Astron. Astrophys.* **687** (2024) A183, [[2405.09184](#)].
- [52] S. Mei, J. Blakeslee, P. Cote, J. Tonry, M. J. West, et al., *The ACS Virgo Cluster Survey. 13. SBF Distance Catalog and the Three-Dimensional Structure of the Virgo Cluster*, *Astrophys. J.* **655** (2007) 144–162, [[astro-ph/0702510](#)].
- [53] M. Di Mauro, J. Pérez-Romero, M. A. Sánchez-Conde, and N. Fornengo, *Constraining the dark matter contribution of γ rays in clusters of galaxies using Fermi-LAT data*, *Phys. Rev. D* **107** (2023), no. 8 083030, [[2303.16930](#)].
- [54] P. Charlot, C. S. Jacobs, D. Gordon, S. Lambert, A. de Witt, et al., *The third realization of the International Celestial Reference Frame by very long baseline interferometry*, *A&A* **644** (Dec., 2020) A159, [[2010.13625](#)].
- [55] E. L. Lokas and G. A. Mamon, *Properties of spherical galaxies and clusters with an n_{fw} density profile*, *Mon. Not. Roy. Astron. Soc.* **321** (2001) 155, [[astro-ph/0002395](#)].
- [56] **Event Horizon Telescope, Fermi Large Area Telescope, H.E.S.S., MAGIC, VERITAS, EAVN**, J. C. Algaba et al., *Broadband multi-wavelength properties of M87 during the 2018 EHT campaign including a very high energy flaring episode*, *Astron. Astrophys.* **692** (2024) A140, [[2404.17623](#)].
- [57] M. Girardi, D. Fadda, G. Giuricin, F. Mardirossian, M. Mezzetti, et al., *Velocity dispersions and x-ray temperatures of galaxy cluster*, *Astrophys. J.* **457** (1996) 61–76, [[astro-ph/9507031](#)].
- [58] A. Longobardi, A. Boselli, S. Boissier, S. Bianchi, P. Andreani, et al., *The GALEX Ultraviolet Virgo Cluster Survey (GUViCS). VIII. Diffuse dust in the Virgo intra-cluster space*, *A&A* **633** (Jan., 2020) L7, [[2001.05512](#)].
- [59] K. D. Gordon, G. C. Clayton, K. A. Misselt, A. U. Landolt, and M. J. Wolff, *A Quantitative Comparison of the Small Magellanic Cloud, Large Magellanic Cloud, and Milky Way Ultraviolet to Near-Infrared Extinction Curves*, *ApJ* **594** (Sept., 2003) 279–293, [[astro-ph/0305257](#)].
- [60] A. Ayala, I. Domínguez, M. Giannotti, A. Mirizzi, and O. Straniero, *Revisiting the bound on axion-photon coupling from Globular Clusters*, *Phys. Rev. Lett.* **113** (2014), no. 19 191302, [[1406.6053](#)].

- [61] S. Porras-Bedmar, M. Meyer, and D. Horns, *Novel bounds on decaying axionlike particle dark matter from the cosmic background*, *Phys. Rev. D* **110** (7, 2024) 103501, [[2407.10618](#)].
- [62] D. Wadekar and Z. Wang, *Strong constraints on decay and annihilation of dark matter from heating of gas-rich dwarf galaxies*, *Phys. Rev. D* **106** (2022), no. 7 075007, [[2111.08025](#)].
- [63] B. Bolliet, J. Chluba, and R. Battye, *Spectral distortion constraints on photon injection from low-mass decaying particles*, *Mon. Not. Roy. Astron. Soc.* **507** (2021), no. 3 3148–3178, [[2012.07292](#)].
- [64] G. Cowan, K. Cranmer, E. Gross, and O. Vitells, *Asymptotic formulae for likelihood-based tests of new physics*, *Eur. Phys. J. C* **71** (2011) 1554, [[1007.1727](#)]. [Erratum: *Eur.Phys.J.C* 73, 2501 (2013)].
- [65] J. E. O’Donnell, *R v-dependent Optical and Near-Ultraviolet Extinction*, *ApJ* **422** (Feb., 1994) 158.
- [66] T. S. Poole et al., *Photometric Calibration of the Swift Ultraviolet/Optical Telescope*, *Mon. Not. Roy. Astron. Soc.* **383** (2008) 627–645, [[0708.2259](#)].
- [67] **HAWC**, A. Albert et al., *Search for decaying dark matter in the Virgo cluster of galaxies with HAWC*, *Phys. Rev. D* **109** (2024), no. 4 043034, [[2309.03973](#)].
- [68] G. C. Perola and M. Tarenghi, *IUE spectra of the jet and the nucleus of M 87.*, *ApJ* **240** (Sept., 1980) 447–454.
- [69] “IUE Newly Extracted Spectra (INES).” <https://sdc.cab.inta-csic.es/ines/index2.html>. Accessed: 2025-06-17.